ORIGINAL RESEARCH

TME-Activated MnO$_2$/Pt Nanoplatform of Hydroxyl Radical and Oxygen Generation to Synergistically Promote Radiotherapy and MR Imaging of Glioblastoma

Lijuan Chen [1],*, Mingbo Liu[2],*, Yunjuan Wang[3,4],*, Wei Wei[1], Yaqiong Li[5], Yan Bai[1], Xuan Yu[1], Lei Jiao[6], Meiyun Wang[1,4]

[1]Department of Medical Imaging, Henan Provincial People's Hospital & the People's Hospital of Zhengzhou University, Zhengzhou, Henan, 450003, People's Republic of China; [2]Department of Radiotherapy, Henan Provincial People's Hospital & the People's Hospital of Zhengzhou University, Zhengzhou, Henan, 450003, People's Republic of China; [3]School of Life Sciences, Henan University, North Section of Jinming Avenue, Kaifeng, Henan, 475004, People's Republic of China; [4]Institute of Biomedicine, Henan Academy of Sciences, Zhengzhou, Henan, 450046, People's Republic of China; [5]Department of Pharmacy, Henan Provincial People's Hospital & the People's Hospital of Zhengzhou University, Zhengzhou, Henan, 450003, People's Republic of China; [6]Institute of Molecular Metrology, College of Chemistry and Chemical Engineering, Qingdao University, Qingdao, Shandong, 266071, People's Republic of China

*These authors contributed equally to this work

Correspondence: Meiyun Wang, The Department of Medical Imaging, Henan Provincial People's Hospital & the People's Hospital of Zhengzhou University, No. 7, WeiWu Road, Zhengzhou, Henan, 450003, People's Republic of China, Email mywang@zzu.edu.cn

Purpose: Radiotherapy (RT) is currently recognized as an important treatment for glioblastoma (GBM), however, it is associated with several challenges. One of these challenges is the radioresistance caused by hypoxia, whereas the other is the low conversion efficiency of the strongly oxidized hydroxyl radical (•OH), which is produced by the decomposition of water due to high-energy X-ray radiation. These factors significantly limit the clinical effectiveness of radiotherapy.

Results: To address these limitations, we developed a highly stable and efficient nanoplatform (MnO$_2$/Pt@BSA). Compared to MnO$_2$@BSA, this platform demonstrates high stability, a high yield of oxygen (O$_2$), enhanced production of •OH, and reduced clearance of •OH. The system exhibited increased O$_2$ production in vitro and significantly improved oxygen production efficiency within 100 s at the Pt loading of 38.7%. Furthermore, compared with MnO$_2$, the expression rate of hypoxia-inducible factor (HIF-1α) in glioma cells treated with MnO$_2$/Pt decreased by half. Additionally, the system promotes •OH generation and consumes glutathione (GSH), thereby inhibiting the clearance of •OH and enhancing its therapeutic effect. Moreover, the degradation of the nanoplatform produces Mn^{2+}, which serves as a magnetic resonance imaging (MRI) contrast agent with a T$_1$-weighted enhancement effect at the tumor site. The nanoplatform exhibited excellent biocompatibility and performed multiple functions related to radiotherapy, with simpler components. In U87 tumor bearing mice model, we utilized MnO$_2$/Pt nanocatalysis to enhance the therapeutic effect of radiotherapy on GBM.

Conclusion: This approach represents a novel and effective strategy for enhancing radiotherapy in gliomas, thereby advancing the field of catalytic radiotherapy and glioma treatment.

**Keywords:** radiotherapy, glioblastoma, MnO$_2$/Pt@BSA nanoplatform, nanocatalysis

Introduction

Glioblastoma (GBM) is considered one of the most malignant primary intracranial tumors, however, the survival rate of patients with GBM has remained largely unchanged in recent decades.[1] Radiotherapy (RT) is a crucial component of the treatment of local GBM. Despite the significant advancements in RT, several challenges persist.[2] One such challenge is the insufficient efficiency of the strongly oxidized hydroxyl radical (•OH), which is produced by the decomposition of water due

to high-energy X-ray radiation,[3] and another challenge is the complex tumor microenvironment (TME), such as hypoxia, which is associated with increased radioresistance in GBM.[4] In addition, the highly toxic •OH produced by ionizing radiation can be eliminated by overexpressing glutathione (GSH) in tumor cells (the concentration of GSH is approximately 1–2 mM in normal cells and up to 10 mM in tumor cells),[5] further aggravating the deficiency of •OH, resulting in insensitivity to various reactive oxygen species (ROS) treatments as well as radiotherapy. Therefore, it is necessary to simultaneously increase the oxidative stress and overcome the hypoxic environment at the tumor site for radiotherapy.[6]

In recent years, a number of strategies have been explored to enhance the effectiveness of radiotherapy based on nanotechnology, aiming to increase oxidative stress and reduce tumor hypoxia, owing to their advantageous performance in biomedical applications and their ability to exploit the biological characteristics of tumors.[7,8] Oxygen supplementation is the most direct and effective method for alleviating hypoxia.[9] Among them, hyperbaric oxygen inhalation,[10] oxygen-carrying perfluorocarbon nanodroplets, oxygenated hemoglobin,[11] or photothermal therapy can be used to enhance blood flow into the tumor and further improve overall tumor oxygenation.[12] However, these methods have the disadvantage of not being easily controlled and being unstable during systematic delivery, which results in unobvious reoxygenation of tumor cells. With the development of oxygen-generating materials, in situ O_2-producing nanoplatforms have been designed and prepared for oxygen supply, which take advantage of tumor-specific microenvironment characteristics (ie, higher levels of H_2O_2 and weakly acidic pH),[13] such as Mn-based,[14,15] Fe-based,[16] and other noble metal-based nanoplatform. Among them, MnO_2, especially its nanosheet morphology, has been widely studied for its peroxidase-like activity in O_2-production, and the binding or loading capacity of drugs[17] and photosensitizers.[18] Prasad et al first fabricated bioinorganic nanoparticles composed of polyelectrolyte-albumin and MnO_2 complex nanoparticles (albumin-MnO_2) to regulate the TME and enhance radiation response in cancer treatment.[14] However, the catalytic activity of single-component MnO_2 nanosheets is low,[19] and to overcome the low catalytic activity of MnO_2 nanosheets, they may be combined with other nanoparticles. Many Mn-based nanoplatform combined with high-Z elements have been developed to alleviate hypoxia and physically enhance RT, such as Hf,[20] Au, and Pt,[21,22] which not only contribute to the catalytic activity of the Mn-based nanoplatform but can also absorb high radiation doses within tumors to facilitate tumor removal at RT. Among these high-Z radiosensitizers, platinum-based radiotherapy sensitization has achieved multifunctional applications beyond the deposition of radiation energy; for example, it has been demonstrated that Pt_2Au_4 clusters,[23] porous Pt nanoparticles,[24] and $Pt(0)/Pt^{2+}$ nanoassemblies[25] are not only able to significantly increase radiation-induced DNA damage and ROS stress by effectively emitting electron radiation after interaction with X-rays within cancer cells, but also exhibit peroxidase-like activity, which regulates tumor hypoxia and enhances the efficacy of radiotherapy through the sustained production of O_2 by endogenous H_2O_2 decomposition. Furthermore, based on degradable materials, MnO_2 is more easily reduced by endogenous glutathione (GSH), leading to GSH depletion and preventing GSH from scavenging toxic hydroxyl radicals (•OH), thereby further amplifying oxidative stress.[26] Crucially, the fact that GSH is more readily consumed by MnO_2 indicates that MnO_2 has higher reactivity with GSH than H_2O_2. Consequently, Mn^{2+} initiated a Fenton-like reaction that generated additional •OH radicals. This process makes the chemical reaction more probable from a cascade dynamics perspective, thereby enhancing the overall mechanism of oxidative stress.

Herein, we hypothesized that MnO_2/Pt can attenuate tumor hypoxia and lead to favorable cancer treatment outcomes in glioma radiation therapy in different ways, including increased oxygen production efficiency, increased energy deposition, increased •OH production, and inhibition of •OH scavenging (Scheme 1). MnO_2 possesses catalase-like nanozyme activity, responds to the tumor microenvironment (H^+ and H_2O_2), and serves as a biodegradable nano-platform for oxygen generation. Mn^{2+}-mediated magnetic resonance imaging (MRI) can be used for image-guided RT.[27,28] As an advanced catalase-like nanozyme, platinum exhibits strong X-ray or gamma-ray attenuation capability, precipitating radiation energy within tumors and improving the radiotherapeutic efficiency.[29] Furthermore, Pt can efficiently decompose H_2O_2 and generate O_2. In addition, Mn^{2+}-mediated Fenton-like reactions for chemo-dynamic therapy (CDT) can be an effective supplement to inadequate intracellular hydroxyl radical production. Moreover, we utilized template-free synthesis, which may be an alternative method to remove the template for most of the reported high-Z metallic frameworks or coordination. To this end, we developed a well-dispersed MnO_2/Pt dual-component nanoplatform, integrating platinum into manganese dioxide (MnO_2), based on our previous research and a substantial body of literature.[30–32] This system, with its simple composition and economical preparation method, can be preserved for an extended period after dispersion in bovine serum albumin (BSA). This is expected to play a significant role in the clinical enhancement of RT.

11056
DovePress

International Journal of Nanomedicine 2024:19
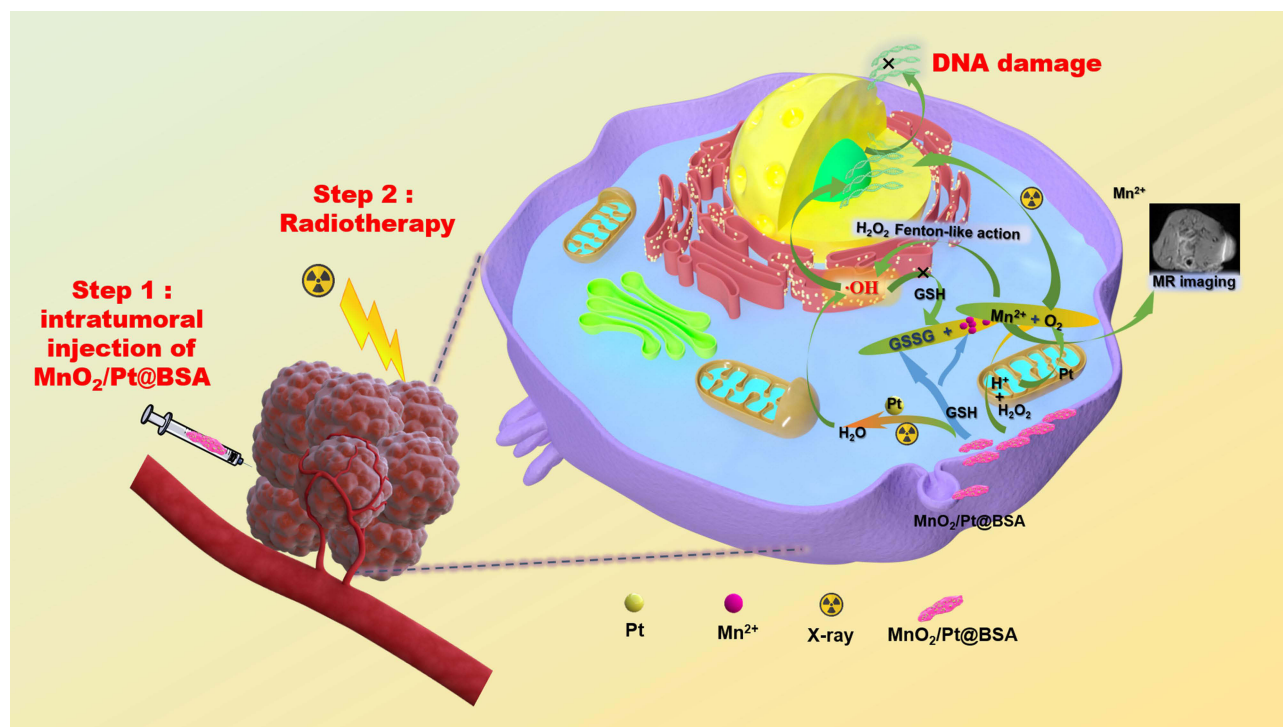
Scheme I Schematic illustration of the application of MnO$_2$/Pt nanoplatform of glioblastoma therapy.

Materials and Methods
Materials

Potassium permanganate (KMnO$_4$) and glucose were obtained from Yantai Luoyang Chemical Reagent Factory. Chloroplatinic (IV) acid hexahydrate (H$_2$PtCl$_6$·6H$_2$O), methylene blue (MB), and glutathione (GSH) were purchased from MACKLIN. NaHCO$_3$, MnCl$_2$, 30% H$_2$O$_2$ and NH$_3$·H$_2$O were purchased from Tianjin Zhiyuan Reagent Co., Ltd., and BSA was obtained from BioFroxx. 3-(4,5)-dimethylthiahiazo (-z-y1)-3,5-di-phenytetrazoliumromide (MTT) was procured from NCM Biotech and [Ru(dpp)$_3$] Cl$_2$ (RDPP) was ordered from Alfa Aesar, hypoxia inducible factor-1α (HIF-1α) were obtained from Novus Bio-Techne China Co., Ltd. Crystal violet was purchased from Tianjin Kemiou Chemical Reagent Co., Ltd. and γ-H2AX was obtained from ServiceBio. The water was deionized using a water purification system (Simple-Q15, Zhi Ang, China). All chemical reagents were purchased from commercial suppliers and used without further purification. All materials used were of analytical reagent (AR) grade and were used as received.

Cell Lines and Animals

U87 cells were purchased from iCell Bioscience Inc. (Shanghai, China). And cells were cultured in Dulbecco's modified Eagle's medium (DMEM; Hyclone) supplemented with 10% fetal bovine serum (FBS; Gibco). The cells were maintained in a humidified incubator at 37 °C with 95% air and 5% CO$_2$. Specific Pathogen-Free (SPF) BALB/c-nu mice ordered from the Charles River (Beijing) were fasted for the establishment of U87-tumor based models and further for the in vivo anti-tumor therapeutic studies. Biosafety studies were conducted using BALB/c mice after acclimatization them for one week. This study was approved by the Experimental Animal Care and Use Ethics Committee of the Henan Institute of Traditional Chinese Medicine, and all the animal experiments were performed in accordance with its guidelines (No: HNTCMDW-20191103).

Methods
Preparation of MnO$_2$, MnO$_2$/Pt MnO$_2$@BSA and MnO$_2$/Pt@BSA Nanoplatform

First, 1 mL potassium permanganate (KMnO$_4$, 5 mg/mL) was added to 30 mL glucose solution (1 mg/mL) at 60 °C. Then, 20 μL of 25% NH$_3$·H$_2$O was added after the solution was well mixed for 2 min, and with H$_2$PtCl$_6$·6H$_2$O (0.1 M,

100 μL) followed by adding in and another stirring was continued for 15 min, and the resulting precipitate was purified by deionized water and lyophilized. To obtain more stable samples for biological applications, we used equivalent amounts of BSA as a stabilizer and dispersed them using an ultrasonic cell crusher instrument for 10 min with a work/interval time of 5s/8s a power of 35% (JY96-IIN, NINGBO SCIENTZ BIOTECHNOLOGY CO., LTD). Stability tests were conducted at room temperature (25 °C) and 4 °C comparison between MnO_2, MnO_2/Pt, $MnO_2@BSA$, and $MnO_2/Pt@BSA$ dispersed aqueous solutions with photos recorded regularly.

Characterization of $MnO_2/Pt@BSA$ Nanoplatform

For the prepared $MnO_2/Pt@BSA$ nanoparticles with different proportions (MnO_2 : Pt), the particle size and polydispersity index (PDI) were measured using a laser diffraction particle sizer (Malvern Nano-ZS 90). Transmission electron microscopy (TEM, JEM2100, JEOL Ltd., Japan) with energy-dispersive X-ray spectroscopy (EDS) was used to investigate the microstructure and compositional distribution of the nanoparticles. Full scan and $C1_S$ X-ray photoelectron spectroscopy (XPS) spectra of the MnO_2/Pt nanoparticles were obtained using an XSAM800 multifunctional surface analysis electron spectrometer (Kratos, UK). Fourier transform infrared spectroscopy (FTIR) spectra (KBr) were obtained using a Nicolet iS5 spectrometer (Thermo Scientific, USA). X-ray diffraction (XRD) was conducted from 10 to 80° (D8 Advance, Germany). Electron paramagnetic resonance spectroscopy (EPR, BrukerA300, Germany) was used to detect ·OH production after adding the capturing agent 5.5-dimethyl-1-pyrroline N-oxide (DMPO) with H_2O_2 as a control. All UV-vis spectra and absorbance values were recorded using a multimode microplate reader (Synergy H1, BioTek). All results, including size and PDI, were the means of three test runs under the corresponding assessment conditions.

Hydroxyl Radical Production

Hydroxyl radical production by Mn^{2+}-mediated Fenton-like catalyze reaction were conducted under the HCO_3^- (25 mM) conditions, containing 10 μg/mL, 8 mM H_2O_2, and 0.5 mM $MnCl_2$ for 30 min at 37 °C, the UV-Vis absorption spectrums were determined subsequently. The scavenging of ·OH were tested with/without 10 mM GSH.[33]

Cytotoxicity

To determine the cytotoxicity and validity at the cellular level, an MTT assay was conducted on U87 cells (iCell Bioscience Inc, Shanghai, China). $3×10^3$ cells/well were incubated in 96-well plates in 100 μL of DMEM with Fetal bovine serum (Thermo scientific, USA), in the incubator for 24 h, 100 μL of the solutions at various concentrations were added in a complete DMEM medium. After 36 h of incubation, 20 μL of MTT (5 mg/mL in N. S., Natrii Chloride) was added to each well and further incubated for 4 h. The liquid medium was then replaced with 160 mL of dimethyl sulfoxide (DMSO). Finally, optical density (OD) was measured using a multimode microplate reader (Synergy H1, BioTek) at 570 nm (n=6). The anticancer activities of $MnO_2@BSA$ and $MnO_2/Pt@BSA$ were assessed in the U87 cell line using an MTT assay.

Extracellular and Intracellular O_2 Evolution in Response to H_2O_2

To assess extracellular O_2 generation, a commercial probe ($[Ru(dpp)_3] Cl_2$, (RDPP)) was used to detect fluorescence intensity, which was quenched by oxygen. Briefly, RDPP (3 μL, 10 mM in ethanol) and $MnO_2@BSA$ or $MnO_2/Pt@BSA$ (100 μL) solutions were added to the 96-well plates. After the addition of H_2O_2 (100 μL, pH5.5), the fluorescence spectrum was recorded using a multimode microplate reader (Synergy H1, BioTek) at (λ_{ex} = 488 nm and λ_{em} = 628 nm). H_2O_2 in acetic acid/sodium acetate buffer (pH5.5) as control.

Intracellular oxygen levels were monitored. First, U87 cells ($5 ×10^4$ cells/dish) were seeded into 6-well plate which with coverslips paving in advance for incubation for 24 h. Then, cells were incubated with RDPP (0.1 μM in DMEM medium) for another 4 h. Subsequently, the cells were washed three times with Phosphate Buffered Saline (PBS) and further incubated with 1 mL of $MnO_2@BSA$, $MnO_2/Pt@BSA$ solutions for 24 h, then exposed to 3 mM H_2O_2 in a DMEM medium for 45 min at 37 °C after washing three times. Untreated cells were used as controls. Finally, the cells

were washed thrice and fluorescence images were obtained using an inverted IX70 microscope (OLYMPUS, JAPAN) at an excitation wavelength of $\lambda = 480 \pm 40$ nm.

Immunofluorescence of HIF-1α staining: To evaluate the hypoxia level in tumors, MnO_2@BSA and MnO_2/Pt@BSA treated mice were sacrificed, and the tumor tissues were continuously frozen and fixed in 4% neutral buffered formalin. After washing thrice with PBS (5 min/time), the sections were placed in a repair box filled with citric acid antigenic repair buffer (pH 6.0) in a microwave oven for antigenic repair. The samples were then washed with PBS three times (5 min/time), after which the autofluorescence quenching agent was added and the solution was rinsed under running water for 10 min and blocked with 5% BSA for 30 min, and then incubated with mouse monoclonal HIF-1α antibody (1:50, diluted with 3% BSA) overnight at 4 °C, washed with PBS three times. Finally, with the goat anti-mouse Cy3-labeled antibody (1:300, 3% BSA dilution) for 50 min, and eventually with 4',6-diamidino-2-phenylindole (DAPI, 1:5000) positioning and the fluorescence quenching agent sealing the pieces, and processed routinely, immunofluorescence was imaged using Case Viewer (Wuhan Servicebio Technology Co., LTD), and the positive rate was calculated using the ImageJ software.

MRI Properties Measurements

In vitro MRI: MRI was performed using a 1.5 T clinical MRI scanner (Siemens, Germany). T1-weighted MR images were acquired with magnetic field intensity of 1.5T, Spin echo sequence: TR=16 ms, TE=2.5 ms, the longitudinal (T1) phantom images as well as relaxation time (T1) of MnO_2/Pt@BSA in neutral /acidic (pH 7.4, pH 6.8, pH 5.5) reduced GSH were imaged at different Mn concentration (0.23, 0.12, 0.056, 0.028, 0.014, 0.007,0.003 μM).

In vivo MRI were performed on the U87 tumor-bearing mouse model. The mice were imaged before (0 min) and after intravenous injection 1h and 2h of N.S, $MnCl_2$ and MnO_2/Pt@BSA ([Mn] 0.25 mmol/kg). We examined the relaxation properties of MnO_2/Pt@BSA to investigate its capacity to serve as a contrast agent for T1-weighted MR images using a 3.0 T MRI scanner (uPMR®790, UNITED IMAGING, CHINA, slice orientation: axial and coronal plane) equipped with an animal coil. The region of interest (ROI) signal of tumors were obtained to calculate the signal-to-noise ratio (SNR), SNR is the ratio of the mean pixel signal intensity in a ROI to the standard deviation of the pixel signal intensity in a noisy ROI.

Evaluation of Radiation Effects in vitro and in vivo

In vitro cell activity: U87 cells were seeded in a 96-well dish at a density of 5×10^3 cells/well for 24 h. Then, the cells were incubated with MnO_2@BSA or MnO_2/Pt@BSA (100 μg/mL, 100 μL) for 4 h. Subsequently, the cells were exposed to an X-ray Irradiator (Clinac23EX, VARIAN, USA) at doses of 6, 8, 10, and 12 Gy. After 6 h, cells activity was determined using MTT staining, as described above.

In vitro clonogenic survival assay: U87 cells were seeded in a 6-well dish at a density of 5×10^4 cells/well for 24 h. Then, the cells were incubated with MnO_2@BSA or MnO_2/Pt@BSA (100 μg/mL, 100 μL) for 12 h. Then, the cells were exposed to an X-ray irradiator at doses of 6, 8, 10, and 12 Gy. The cells in the control group were treated with the same parameters in the absence of MnO_2@BSA orMnO_2/Pt@BSA. After 1 h, cells were washed with PBS and the cells were fixed with paraformaldehyde (4 °C, 60 min) and then washed with PBS, and stained with crystal violet staining solution (0.5%, Kemiou Chemical Reagent) for statistical analysis.

γ-H2AX (Servicebio Technology Co., LTD) immunochemistry analysis in vivo: to evaluate DNA damage after different treatments. U87 subcutaneous tumor model (tumor diameter reach 8–10 mm) was established. Treatment with a combination of RT (10 Gy) and MnO_2@BSA or MnO_2/Pt@BSA (i.t). with saline as a negative control. Furthermore, for the negative control, only half of the tumors were irradiated to determine the effect of treatment alone in the same mice. 24 h post-irradiation, tumor tissues were excised and stained with γ-H2AX to evaluate DNA damage with blue stained nuclei. Slides were scanned with a case viewer and images were analyzed using ImageJ software.

Therapeutic Study in Tumor-Bearing Mouse Model

The radiation treatment in vivo: after acclimatization for one-week, SPF Balb/C-nu mice were subcutaneously injected with the U87 (5×10^7 cells/mL, 100 μL) cells. When the tumor diameter reached approximately 8–10 mm, tumor-bearing mice were grouped into six groups (1. Normal saline -N. S; 2. RT Only; 3. MnO_2@BSA; 4. MnO_2/Pt@BSA; 5. MnO_2@BSA + RT, 10Gy; 6. MnO_2/Pt@BSA + RT, 10Gy). For the RT group (Groups 5 and 6), 6h after intravenous

injection of 50 µL (Pt: 2 mg/kg) MnO_2@BSA or MnO_2/Pt@BSA, irradiation with X-rays was performed. The tumor length and width were measured using a caliper rule until the test completed and record the weight of the excised tumor tissue at the endpoint of experiment for effectiveness evaluation. The body weights of the mice were recorded for toxicity evaluation. The tumor volume was calculated using the equation $V = ab^2/2$ (a = length, b = width).

At the 12th day (the endpoint of experiment), the mice were euthanized, and the main organs were harvested for hematoxylin and eosin (H&E) staining for pathological and toxicological analysis. Similarly, the tumor immunohistochemistry biopsy samples of Ki67 and terminal deoxynucleotidyl transferase dUTP nick end labeling (TUNEL) staining were further proliferation and apoptotic index evaluation, the stained specimens were observed with Case Viewer (Wuhan Servicebio Technology Co., LTD).

Blood Analysis and Histology Examinations

Nine healthy Balb/c mice randomly divided into three groups (three mice in each group) were intravenously injected with MnO_2@BSA and MnO_2/Pt@BSA at a dose of 20 mg/kg and sacrificed at the 14th days post injection, saline as control.

At the 1st, 7th, 14th days, the mice were anesthetized and sacrificed, collect 0.1 mL blood in an anticoagulant tube for CBC (BC-2800vet, Mindray, China). The others were centrifuged at 1200 rpm for 15 min to obtain serum for blood chemistry tests, including liver and renal function tests (AST, ALT, ALP, TP, CRE, and BUN) (Chemray 240, Rayto, China). Finally, the main organs of the mice (the heart, liver, spleen, lungs, and kidneys) were harvested and fixed with 4% neutral paraformaldehyde. The tissue samples were embedded in paraffin, sliced (4 µm), and stained with H&E. All the biopsy samples were imaged using an optical microscope (Olympus, Tokyo, Japan).

Statistical Analysis

Data are presented as mean ± SD. The cell viability, signal intensity, and positive ratio of HIF-α, γ-H2AX, TUNEL, and Ki67 were compared by two independent sample Student's t-tests or one-way analysis of variance (ANOVA), statistical significance was set at $p < 0.05$ (*$p < 0.05$, **$p < 0.01$).

Results and Discussion

The MnO_2/Pt nanoplatform was synthesized by a method involving the reduction of potassium permanganate ($KMnO_4$) using glucose and $NH_3 \cdot H_2O$, as shown in Figure 1a. To the best of our knowledge, this is the first-time glucose and
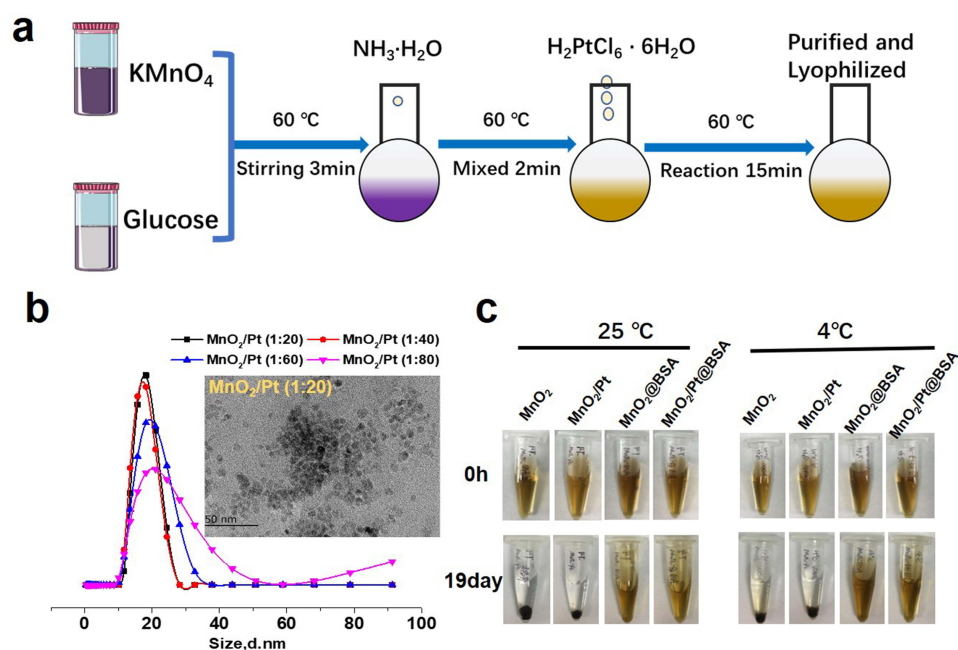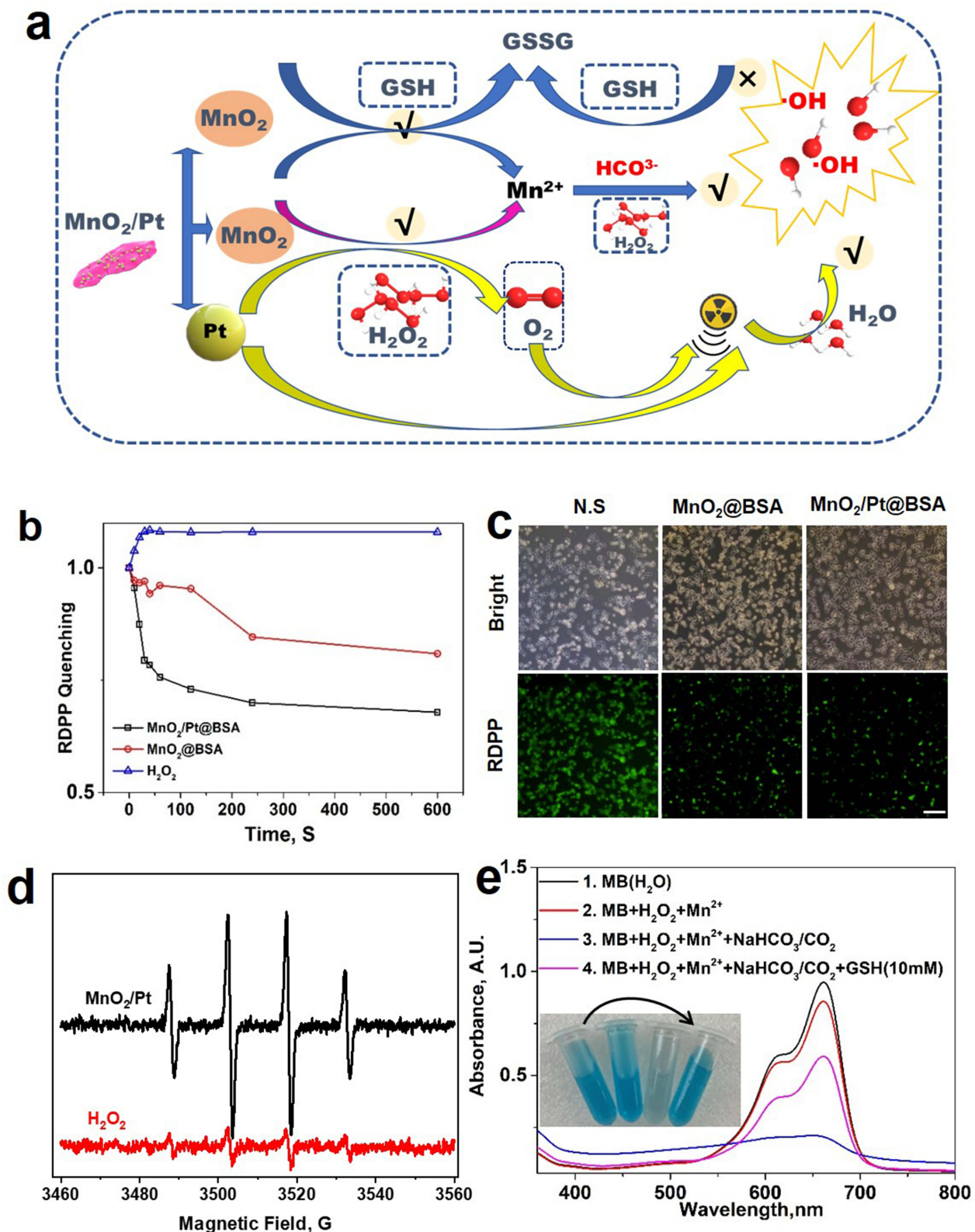

Figure 1 (**a**) Schematic illustration for the processes of the reaction; (**b**) The particle sizes of MnO_2/Pt@BSA and the corresponding TEM image (insert b); (**c**) The storage stability of MnO_2@BSA, MnO_2/Pt@BSA at room temperature (RT) and 4 °C conditions at different timepoints (0h, 19 day).

ammonia have been used as reducing agents for $KMnO_4$. $H_2PtCl_6 \cdot 6H_2O$ (0.1 M, 100 μL) was used as the Pt precursor, and Pt nanoparticles were loaded onto the MnO_2 nanosheets via electrostatic interactions with continued stirring. The color of the reaction solution changed from purple to brown, indicating completion of the reaction after $NH_3 \cdot H_2O$ was added, which took approximately 15 min. The final MnO_2/Pt nanoplatform was obtained. The UV-Vis peak at 530 nm (Figure S1) disappeared after reduction, and a new broad absorbance band at approximately 350 nm emerged, which was attributed to the surface plasmon band of the colloidal manganese dioxide. To achieve a more stable nanoplatform, BSA was used for assisted dispersion using high-intensity ultrasound (Ningbo Scientz Biotechnology Co. LTD). The TEM images (Figure 1b insert and Figure S2a1–a3) and EDS elemental mapping of Pt and Mn (Figure S2b1–b4) demonstrated the successful construction of the MnO_2/Pt@BSA nanoplatform. As the Pt ratio increased, the particle size gradually increased (Figure 1b), from Size 1 with the MnO_2/Pt molar ratios at 1:20 of 17.93 nm, Size 2 (1:40) of 17.41 nm, Size 3 (1:60) of 19.67 nm, to Size 4 (1:80) of 22.55 nm. Considering the stability of the platform, the ratio for application was 1:20 unless otherwise specified. XPS data were used to identify the components of MnO_2/Pt using the corresponding Mn^{IV} 2p1/2 (653.66 eV)/Mn^{IV} 2p3/2 (641.99 eV) and $Pt^0$4f5/2 (76.00 eV)/$Pt^0$4f7/2 (72.64 eV) spectra (Figure S3d and e). According to the characterization analysis, the Pt nanoparticles were distributed on the MnO_2 sample, which enhanced its catalytic performance.[34] The Pt loading efficiency of MnO_2 was determined to be 38.7 wt % using inductively coupled plasma emission spectroscopy (ICP-MS, Agilent, ICPOES730). Catalase (CAT)-like activity of Pt showed a stronger concentration dependence, which suggests that low concentrations of Pt have weaker catalase activity.[35] Therefore, high platinum loading is important for oxygen generation throughout the platform.

To enhance the solution stability of MnO_2/Pt, we used BSA as a stabilizer to uniformly disperse the product (MnO_2/Pt@BSA).[36] The collected pictures of MnO_2, MnO_2@BSA, MnO_2/Pt, and MnO_2/Pt@BSA stored at 4 °C and room temperature (25 °C) showed that with the stabilization of BSA, the nanoplatforms were stable at 4 °C for up to 19 days without visible precipitation (Figure 1c and Figure S4). However, flocculent precipitates began to appear in the MnO_2/Pt samples without BSA 1 h after the preparation (Figure S4a). The incubation of MnO_2/Pt in a cell culture medium containing 10% fetal bovine serum (FBS) resulted in a homogeneous, well-dispersed formulation, with no obvious morphological variation (Figure S4b), this indicates a significant improvement in stability.

As shown in Figure 2a, the ultimate goal of the platform is to utilize the catalytic properties of MnO_2/Pt@BSA and synergistically adjuvant radiotherapy to increase the production of oxygen and hydroxyl radicals. With regard to oxygen production, MnO_2/Pt@BSA has demonstrated to be more stable under neutral conditions (pH7.4) regardless of the H_2O_2 exit or not (Figure S5a), whereas it can be reduced to a colorless solution through H_2O_2-facilitated reaction under acidic conditions (pH5.5) (Figure S5a2). For MnO_2/Pt@BSA, a hydrogen peroxide concentration-dependent effect was observed under acidic conditions (pH 6.8), with an increased concentration of hydrogen peroxide, the UV absorption of MnO_2/Pt@BSA gradually decreased (Figure S5b). The decomposition reaction of MnO_2/Pt@BSA was triggered by H_2O_2 and the brown color faded at pH 5.5, owing to the degradation of MnO_2, whereas the absence of H_2O_2 did not cause the reaction to occur under different pH conditions (Figure S5a1–a2). The newly introduced Pt nanoparticles further synergistically promoted O_2 generation via the $2H_2O_2 + Pt \rightarrow O_2 + 2H_2O$ reaction.[37] The in vitro evaluation of oxygen production was carried out using an O_2 probe, $[Ru(dpp)_3] Cl_2$ (RDPP), which can be quenched proportionally by the generated O_2. The RDPP probe was incubated with an acidic H_2O_2 solution (100 mM, pH 5.6), which mimicked the tumor microenvironment.[38] As shown in Figure 2b, the fluorescence intensity of RDPP did not show significant changes upon exposure to 100 mM H_2O_2 (PBS [pH 5.6]) and slightly decreased after exposure to MnO_2. However, the fluorescence intensity of RDPP sharply decreased within 100 s in the MnO_2/Pt@BSA-treated H_2O_2 solution, indicating efficient O_2 generation. Furthermore, compared with the control group, the weakest green fluorescence signals were observed in U87 cells incubated with MnO_2/Pt@BSA, owing to the ability of catalase to react with the overexpressed H_2O_2 in cancer cells, generating a large amount of O_2 that significantly quenched RDPP. In contrast, the mildly weak green emission within the MnO_2/H_2O_2-treated U87 cells was slightly quenched, owing to the generation of a small amount of O_2 (Figure 2c). Hydroxyl radicals (·OH) are among the most reactive types of ROS.[39,40] The ESR spectra of MnO_2/Pt@BSA (Figure 2d) displayed a standard quadruple pattern (four peaks) with equidistant peaks and a peak height of 1:2:2:1, indicating the generation of ·OH using DMPO as a capture agent. Notably, the heights of the peaks suggested a significantly higher concentration of free radicals produced by MnO_2/Pt@BSA than the control group. This is

Figure 2 (**a**) Schematic illustration of various pathways of oxygen (O_2) and hydroxyl radical ($\cdot$OH) generation from MnO_2/Pt@BSA; (**b**) Generation of O_2 under the reduction of MnO_2/Pt@BSA and MnO_2@BSA nanoplatform by H_2O_2 in PBS (pH 5.5); (**c**) The evolution of O_2 in U87 cells by using RDPP (bar=20 μm); (**d**) ESR spectra of the generation of $\cdot$OH after MnO_2/Pt@BSA incubation with H_2O_2 (PBS, pH=6), H_2O_2 as control, wherein DMPO acted as the capturing agent of $\cdot$OH; (**e**) UV-Vis absorption spectra of MB degradation by Mn^{2+} mediated fenton-like reaction with the photograph (insert).

consistent with the experimental results of the free radical detection with the methylene blue (MB) probe in vitro (Figure 2e), which can be attributed to the function of $H_2O_2 + Mn^{2+}/HCO_3^- \rightarrow \cdot OH + 2H_2O$.[41] In addition, highly reactive $\cdot OH$ radicals are generated by radiotherapy. The oxidative damage to tumors caused by $\cdot OH$ can be mitigated by potent reducing agents in the tumor microenvironment, such as GSH.[42] Therefore, depleting GSH levels is also a crucial strategy for enhancing the efficacy of radiotherapy.

Based on the data in Figure 3, $MnO_2/Pt@BSA$ reacted with GSH (5mM, pH 6.8) and degraded within 3 minutes (Figure 3a, insert), leading to a change in color from brown-yellow to colorless. The UV-vis spectrum (300–600 nm) further indicated that $MnO_2/Pt@BSA$ (1 μmol/mL) interacted with different concentrations of GSH (50, 25, 3.12, 1.56, 0.39, and 0 mM) and showed a concentration-dependent degradation pattern. The absorbance exhibited concentration-dependent behavior, with increasing GSH concentration, resulting in a decrease in the absorption value. MRI results indicate that the production formed after the degradation of $MnO_2/Pt@BSA$ is Mn^{2+} which possesses MR imaging ability. Additionally, it displayed a concentration-dependent brightness effect in different acid GSH-rich conditions (pH 5.5/6.8/7.4 + 5 mM GSH), and the corresponding longitudinal relativity r1 value were acquired to be 7.32, 4.78, and 7.11 $mM^{-1}S^{-1}$ in mild acidic and neutral GSH conditions. Under the same conditions but in the absence of GSH, the r1 values were as low as 1.25, 0.59, and
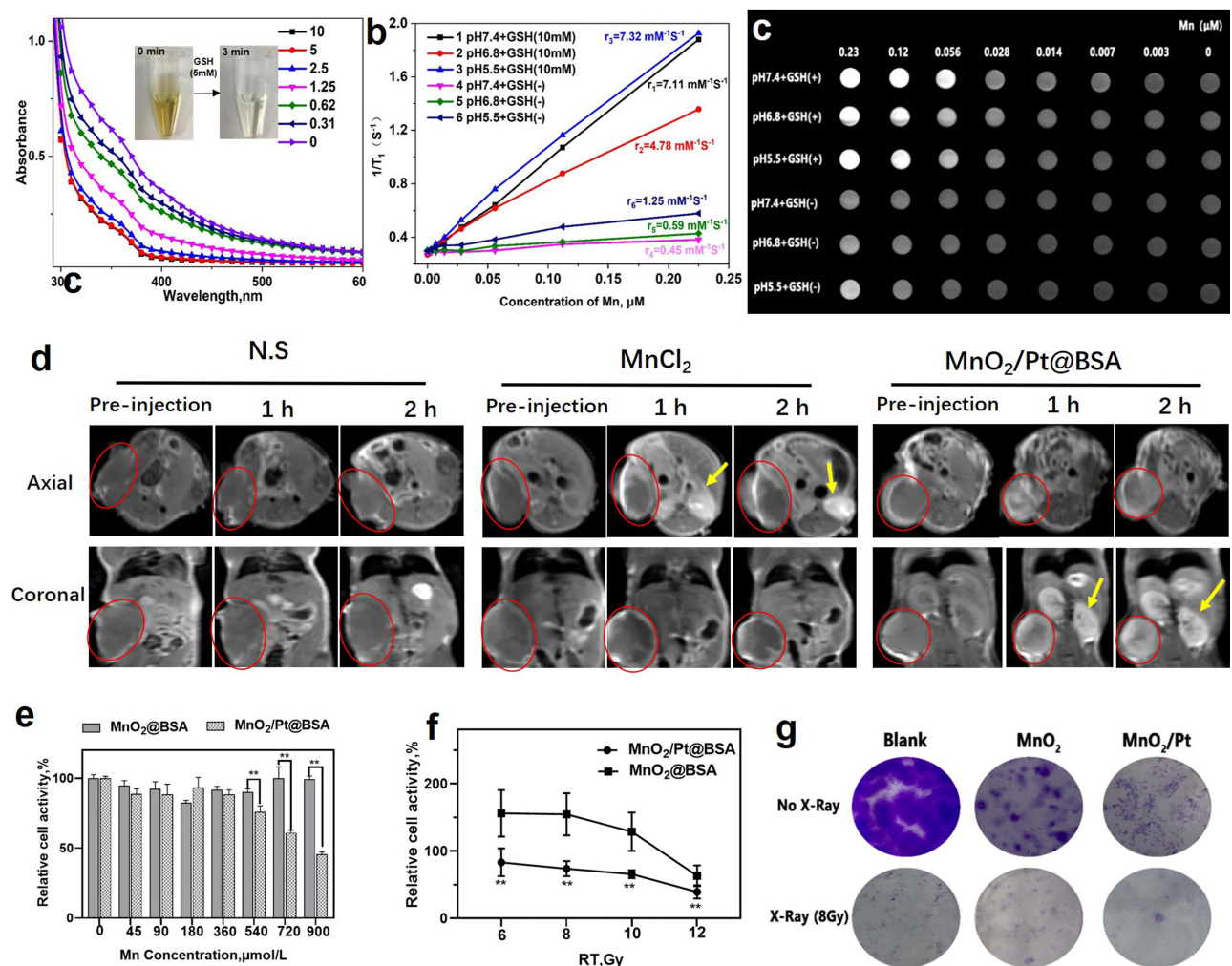

Figure 3 (**a**) The absorbance of $MnO_2/Pt@BSA$ after pH 6.8 at different GSH concentration (50, 25, 3.12, 1.56, 0.39, 0), and the photograph of $MnO_2/Pt@BSA$ degradation within 3 min (insert); (**b**) the corresponding r1 value after treatment with different pH buffer solution and/or not GSH; (**c**) T1-weighted MR imaging of $MnO_2/Pt@BSA$ after GSH(±) treatments with different pH conditions (pH 7.4/6.8/5.5); (**d**) and In vivo study of T1-weighted MR imaging of U87 tumor-bearing mice on a 3.0 T MRI scanner pre-injection (0 min) and after intravenous injection of N.S, $MnCl_2$, and $MnO_2/Pt@BSA$ at the dose of $C[Mn] = 0.25$ mmol·kg^{-1}. (The red circle represents the location of the tumor, and the yellow arrow represents the location of the kidney) (**e**) The relative cell activity (%) of the nanoplatforms on U87 cell lines for cytotoxicity evaluation. (**f**) Relative cell activity (%) of U87 cell lines treated with $MnO_2/Pt@BSA$ or $MnO_2@BSA$ at different dose of X-ray radiation (6, 8, 10, 12 Gy). (**g**) A colony of U87 cells treated with $MnO_2/Pt@BSA$ or $MnO_2@BSA$ combined X-ray radiation (8 Gy). (**p < 0.01).

$0.45 \text{ mM}^{-1}\text{S}^{-1}$ (Figure 3b). Furthermore, the T1-weighted MR images in Figure 3c demonstrated that a stronger enhancement following reduction by GSH and in solutions at pH 5.5/6.8/7.4 with varying Mn concentrations, this indicates that the MnO_2-mediated consumption of GSH could efficiently enhance MRI, whereas, the reactions were insufficient without GSH.[43] Based on the favorable GSH response performance, we investigated its responsiveness in tumors of MnO_2/Pt@BSA. Firstly, 2h after the intratumoral injections of was shown in Figure S6, the tumor site exhibited a relatively high T1-weighted MRI signal compared to the average signal of normal tissue, and there was uneven enhancement characteristics of the MRI signal with intratumoral injection. Furthermore, Figure 3d shown the T1-weighted MR images of $MnCl_2$ and MnO_2/Pt@BSA intravenously injected at the concentration of Mn C[Mn] ($0.25 \text{ mmol·kg}^{-1}$) with N.S as control on U87 tumor-bearing mice model. The corresponding grey scale images clearly shown that the MRI effect of both $MnCl_2$ and MnO_2/Pt@BSA. Specifically, in the axial and coronal imaging pre-injection, there was no enhancement at the tumor site among all groups. 1-hour post-injection of $MnCl_2$, the entire section showed varying degrees of enhancement, with uneven tumor enhancement and notably increased enhancement in both kidneys (transverse section, yellow arrow), which persisted till to the 2h time point. For the MnO_2/Pt@BSA group, it is significant enhancement at the tumor site (red circle) both at the 1h and 2h after injection, while kidney enhancement appeared at 2h. This suggests that MnO_2 was degraded to release $Mn^{2\square}$, which possess MR imaging capabilities and subsequently excreted through the kidneys. The quantitative analysis of percentage growth rate of the tumor T_1 SNR were compared to pre-injection, $MnCl_2$ indicated that $212.2 \pm 22.4\%$ (*$P<0.05$) at 1h post-injection (Figure 3d and Figure S7), which are $190.0 \pm 21\%$ (*$P<0.05$) at 2h post-injection, and $254.7 \pm 26\%$ (**$P<0.01$) at 1h post-injection, $245.7 \pm 12.5\%$ (**$P<0.01$) of MnO_2/Pt@BSA (Figure 3d and Figure S7) compared to the control group of N.S. The satisfactory in vivo MRI results are primarily due to the effective tumor targeting and excellent degradation response performance of MnO_2/Pt@BSA. These results further demonstrate that MnO_2/Pt@BSA are potential candidates for practical applications as T1-weighted contrast agent.

To further enhance the therapeutic effect, the combination of MnO_2 and Pt facilitates not only more efficient O_2 production but also ·OH generation for better tumor cell killing efficacy, while also serving as a T1-weighted contrast agent in vivo. This makes the nanoplatform a promising candidate for enhancing radiotherapy.[44] However, to achieve the status of an ideal multifunctional nanoplatform, biocompatibility is a critical factor to consider, especially due to the presence of two metal elements of Mn and Pt in the composition. First, the relative cell activity (%) of MnO_2/Pt@BSA on 3T3 cell lines was primarily assessed for cytotoxicity evaluation. As shown in Figure S8(a), at the concentrations ranging from 45 to 720 μmol/L of MnO_2/Pt@BSA [Mn] concentration, the viability of 3T3 cells ranged from 74% to 100% compared to the solvent-treated group (Mn concentration: 0 μmol/L). Generally, a viability greater than 70% indicated low toxicity or non-toxicity. Besides, the 3T3 cells exhibited almost identical morphology and good spreading, without obvious morphological shrinkage occurring, regardless of whether the material was treated or not. (Figure S8b and c) For the viability of U87 tumor cells, The results showed that the introduction of Pt in the higher concentration range (Mn: 540–900 μmol/L) significantly reduced the viability of U87 cells to less than 50% (Figure 3e) (**$p < 0.01$). The morphology of cells under a bright field microscope is shown in Figure S9, where the U87 cells crumpled into a round shape and lost their normal morphology after being processed by MnO_2/Pt@BSA nanoplatforms, compared to the saline treatment (Figure S9). Next, the effects of oxygen and free radical (·OH) production on radiotherapy were evaluated at cellular and tissue levels. U87 cells were incubated with MnO_2@BSA and MnO_2/Pt@BSA (100 μM [Mn], corresponding to 20 μM [Pt]) for 4 h and then exposed to X-ray radiation (Clinac23EX, VARIAN, USA) at doses of 6, 8, 10, and 12 Gy. After another day of incubation in fresh cell medium, the relative cell viability was determined using the MTT assay. It was found that the cells treated with MnO_2/Pt@BSA and X-ray exposure exhibited a remarkable decrease in viability compared to cells subjected to MnO_2@BSA treatments (Figure 3f) (**$p < 0.01$). Furthermore, a clonogenic assay was performed, known as a "gold standard" to assess the radiosensitizing effect of a radiosensitizer.[45] As shown in Figure 3g, the photographs demonstrate the degree of colony formation, where pre-treatment with MnO_2@BSA and MnO_2/Pt@BSA without X-ray irradiation improved the survival of cancer cells compared to X-ray (8 Gy) treatment, and the effect of the nanoplatform on the inhibition of cell clonogenesis was also observed. These results suggest that MnO_2@BSA and MnO_2/Pt@BSA have the potential to enhance radiotherapy, with MnO_2/Pt@BSA significantly improving the radiotherapy effect on U87 cells in vitro compared with the radiotherapy and MnO_2@BSA groups.

Therefore, we further investigated the antitumor properties of the MnO_2-based nanoplatform according to the treatment plan shown in Figure 4a. Intratumoral injection was selected to precipitate the radiation energy within the tumors and improve the
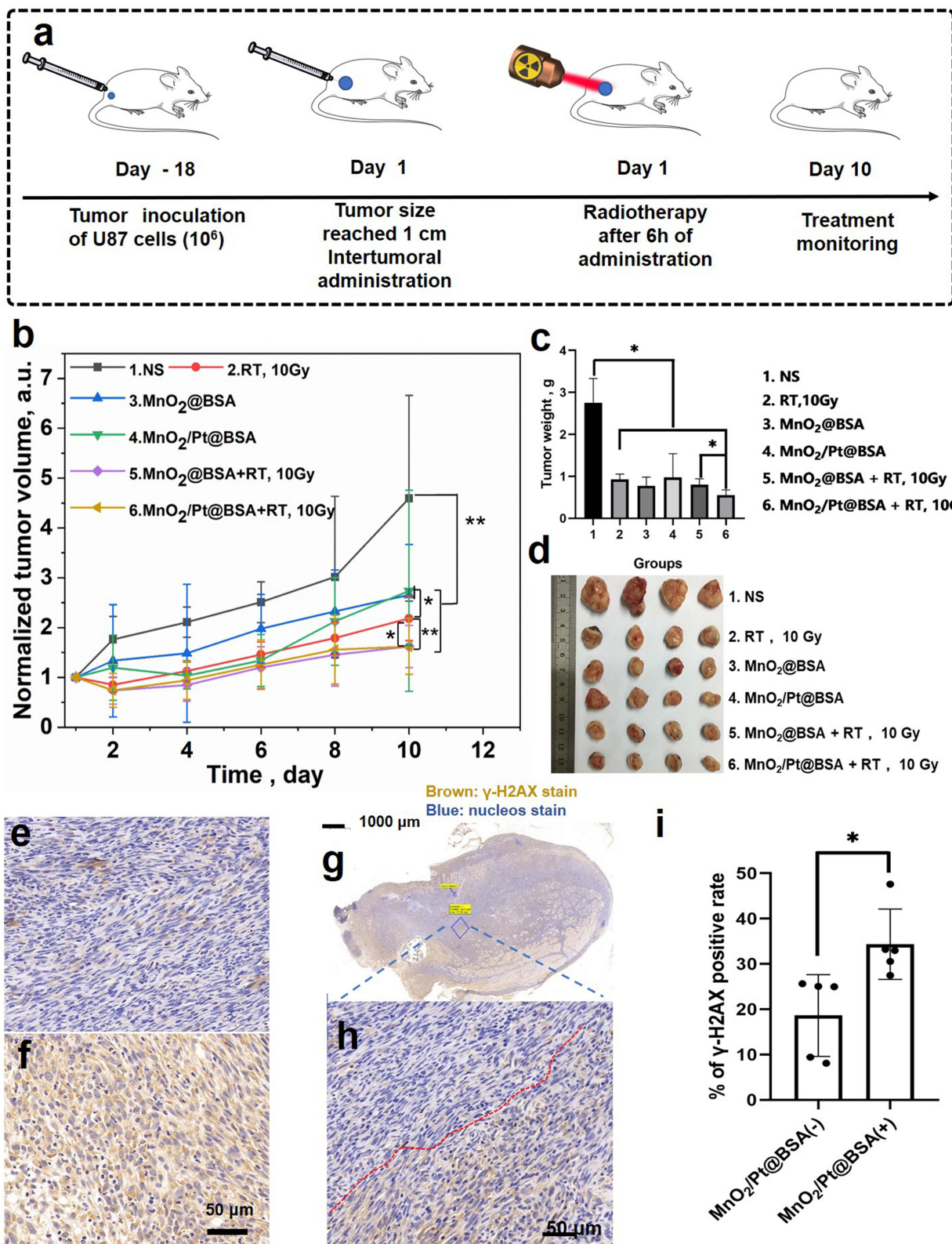
Figure 4 (**a**) The diagram of treatment plan on the U87-tumor-bearing mice model; (**b**) The time-dependent curves of the normalized tumor volume; (**c**) The histogram of tumor weight and (**d**) the photograph of tumors excised from each group; The representative immunohistochemistry in continuous sections from U87 tumors treated i.t. with (**e**) N.S (control) and (**f**) MnO$_2$/Pt@BSA, stained with γ-H2AX (brown), and (**g**) Scan view of the continuous sections from the ex vivo tumor tissue treated with MnO$_2$/Pt@BSA, and the representative enlarged image (**h**) of the boundary of X-ray irradiation (8 Gy). (**i**) The quantification of the corresponding normalized number of γ-H2AX treated with MnO$_2$/Pt@BSA and X-ray irradiation; Results are presented as means±SD. (* stand for significant difference, $p < 0.05$).

radiotherapeutic efficiency. Digital images of the tumors and tumor volume curves for the six groups are shown in Figure 4b–4d. As expected, the group treated with MnO$_2$/Pt@BSA followed by X-ray irradiation achieved the highest tumor growth inhibition, whereas the group treated with MnO$_2$/Pt@BSA alone exhibited an anticancer efficiency equivalent to that of the group treated with radiation therapy only (Figure 4d). These results further suggested that combining MnO$_2$ and Pt is a potent strategy to improve cancer treatment outcomes. Time-dependent normalized tumor volumes of the groups are shown in Figure 4b, both MnO$_2$@BSA and MnO$_2$/Pt@BSA demonstrated tumor-killing capacity compared to the control group (**p < 0.01). It was evident that radiotherapy combined with either MnO$_2$@BSA or MnO$_2$/Pt@BSA achieved a significant anticancer effect, which was much higher than that of radiation therapy alone (10 Gy). Although from the photograph of tumors and the time-dependent curves, there was no significant difference of the average tumor sizes between the groups of MnO$_2$@BSA and MnO$_2$/Pt@BSA. We further analyzed the weight of the dissected tumors of each group, and conducted statistical analysis, we found that there was a significant difference (*p=0.04) in tumor weight between the two groups. The differences in tumor weight maybe due to the internal tumor necrosis or other different types of cell death resulting in differences in tumor weight, which provide the evidence of the effect of Pt, which not only physically enhances radiation therapy but also mediates catalytic oxygen generation. To better understand the effects of different treatments, the extent of DNA damage during radiotherapy was evaluated using γ-H2AX staining (brown), which is a marker of DNA double-strand breaks and genomic instability (Figure 4e–4h and Figure S10). Spatially localized focal X-ray irradiation was performed on half of the tumor tissue pretreated with NS, MnO$_2$@BSA, and MnO$_2$/Pt@BSA. Increased DNA damage was observed when the tumor was treated with RT compared to the other side without X-rays, but only in the nanoplatform in the same U87 solid tumor. For the MnO$_2$/Pt@BSA group, DNA damage (34%) was significantly higher than that in the other parts, with a positive rate of 14% (Figure 4i). The mechanism of radiosensitization by Pt is still not fully understood. However, some studies have suggested that ROS are generated by electron ejection from Pt upon irradiation. When tumor tissues or cells contain a high electron density of heavy elements and are irradiated simultaneously with X-rays, energy transfer and deposition in the tumor tissue can occur, leading to the production of a large number of free radicals and highly charged target atoms. The effects of both DNA and other targets in cells can further increase DNA damage, thus producing a significant sensitizing effect on tumor cells. Cisplatin modification is an efficient means to increase the formation of both single- and double-strand breaks by hydrated electrons and hydroxyl radicals created by ionizing radiation.[46] Therefore, it is highly probable that in addition to oxygen, the increased generation of ·OH in tumor tissue facilitates DNA damage. Furthermore, as GSH is consumed, it becomes increasingly difficult for intrinsic cellular repair mechanisms to function effectively, resulting in increased tumor cell death upon radiation exposure, ultimately leading to a prolonged delay in tumor growth. The widespread clinical use of cisplatin in chemoradiotherapy is due not only to the sensitivity of tumor cells to cisplatin but also to the high-Z material properties of platinum atoms, which have been shown to enhance the effectiveness of radiotherapy.[47,48]

Hematoxylin and eosin-stained (H&E) microscopy images of the tumor sections of the non-treated (N.S) group shown tumor cell invasion in the skeletal muscle and necrosis in the center of the tumor with a pathological mitotic phase of N.S negativity (Figure 5a). In the group treated with radiation therapy alone (group 2, Figure 5a), nuclear dissolution was observed, accompanied by interstitial fibrosis and hyperplasia. In the section with excessive damage, cytoplasmic changes were observed earlier than nuclear changes, and nuclear structure was unclear, with non-uniform necrosis. Vacuities and fibrosis were observed prior to the necrosis. The worst necrosis was observed in group 6, comparative region represents the cells without the nucleus induced by the MnO$_2$/Pt@BSA plus X-ray irradiation, while modest apoptosis occurred in the MnO$_2$@BSA plus X-ray irradiation group (group 5). (Figure 5a) The Ki67 protein can detect a nuclear antigen that is exclusively present in proliferating cells. The expression of Ki67 is indicative of cancer cell proliferation. In this study, the quantification of Ki67 positive cells relative to representative tumor regions was significantly inhibited in groups 4, 5, and 6 compared to that in the NS group (*p < 0.05). Conversely, the other groups, including groups 2 (RT only) and 3 (MnO$_2$), displayed less or milder inhibitory effects (Figure 5a–5b). Furthermore, TdT-mediated dUTP nick end labeling (TUNEL) analysis showed a more wide-extended apoptosis in the group pretreated with MnO$_2$/Pt@BSA or MnO$_2$@BSA and radiotherapy than in the other groups, including the group treated with RT only or without X-ray. Group 6 exhibited a 10.81% TUNEL-positive rate, whereas the other groups showed a significant decrease (*p < 0.01). Group 5 (MnO$_2$@BSA plus X-ray treatment) showed a TUNEL-positive rate of 3.93%, which was significantly higher than that of groups 1–4 (Figure 5c).
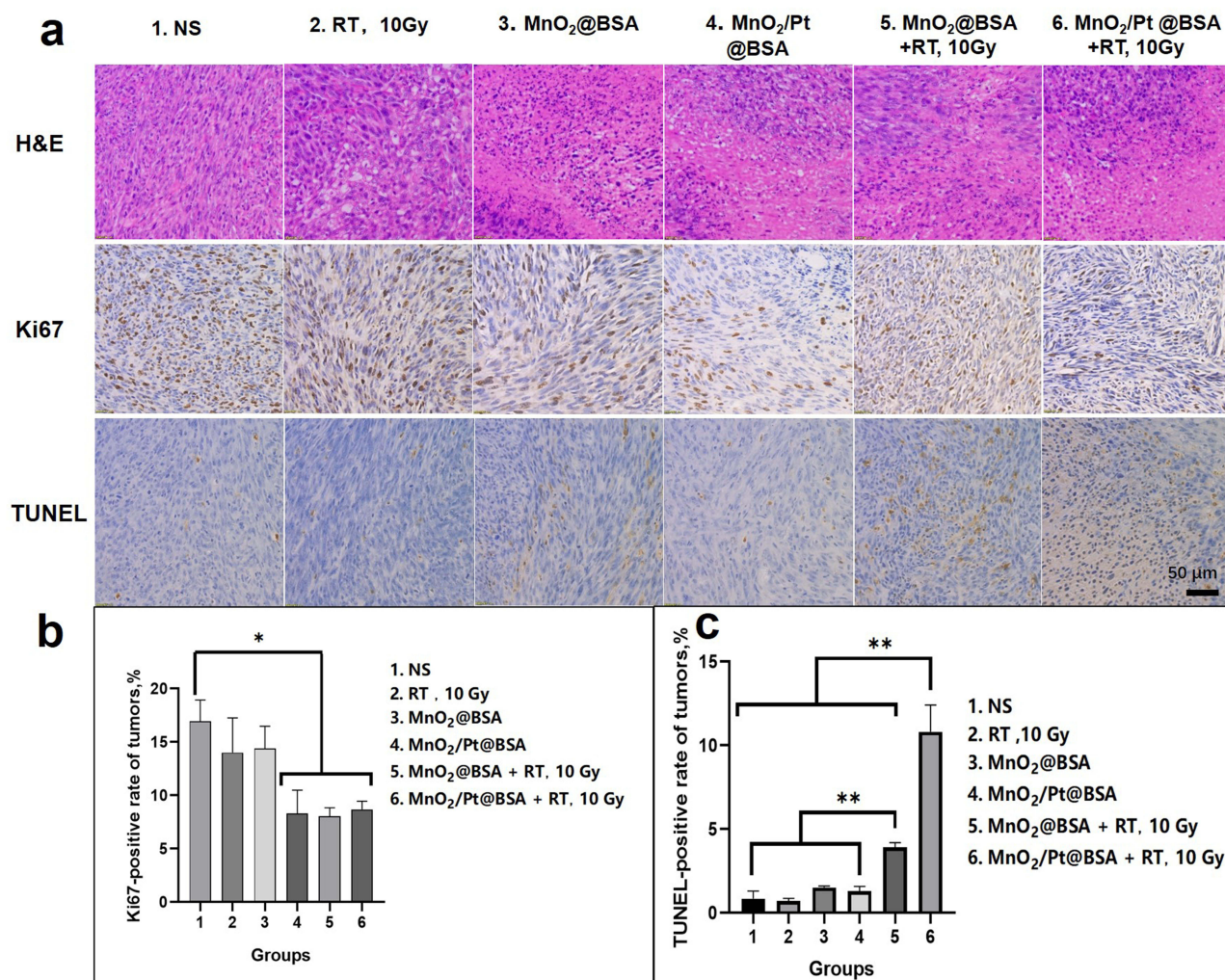
Figure 5 (**a**) The representative H&E, Ki67 and TUNEL immunohistochemical stained microscopy images of the corresponding groups of tumors after the different treatment, saline as control. The positive rate of Ki67 (**b**) and TUNEL (**c**) in different groups (n=5), (*$p < 0.05$, **$p < 0.01$).

MnO$_2$@BSA and MnO$_2$/Pt@BSA in this platform may represent strategies for inhibiting tumors by suppressing HIF-1α expression. Under radiotherapy-treated conditions, the effects of MnO$_2$@BSA and MnO$_2$/Pt@BSA on hypoxic conditions at the tissue level were assessed by measuring the expression of the HIF-1α protein in a U87 tumor-bearing mouse model. The results showed that the expression of HIF-1α was significantly downregulated in the MnO$_2$/Pt@BSA-treated group compared with the saline-treated control group. The positive fluorescence count was quantitatively analyzed, and the positive rate of the MnO$_2$/Pt@BSA-treated group was 4.97± 0.79 (%), which was significantly lower than that of the MnO$_2$@BSA-treated group (8.16 ± 1.86 (%) and the control group (15.63 ± 4.42 (%), indicating efficient MnO$_2$ and Pt-mediated oxygen generation (Figure S11). In this context, O$_2$ generation induced by the MnO$_2$/Pt@BSA nanoplatform was effective in promoting local therapeutic performance in vivo. The MnO$_2$ and Pt supports in this system act as reservoirs that provide oxygen species, whereas in addition to supporting oxygen production, Pt loading enhances the production of ·OH radicals, thus contributing to the overall therapeutic effect.[49] Overall, the addition of Pt to the nanoplatform plays a crucial role in enhancing the therapeutic effect of RT.[50]

After treatment, there were no significant changes in the average body weight of mice in each group throughout the treatment period (Figure S12). This observation indicates that there was no evident toxicity associated with the administration of the nanoplatform. Furthermore, H&E-stained images of the major organs (heart, liver, spleen, lung, and kidneys) of mice treated with MnO$_2$/Pt@BSA by intravenous injection revealed no pathological alterations (Figure S13). The laboratory test results depicted in Figure S14 demonstrate that several indicators, including RBC, MCH, hematocrit, hemoglobin, MCHC,

total protein, blood urea nitrogen, and creatinine (Figure S14b-k), remained within the normal range. However, other indicators such as WBC count, platelet count, ALT, AST, and ALP (Figure S14a, f and h) displayed temporary fluctuations following the intravenous injection of $MnO_2/Pt@BSA$ but returned to normal levels within 7 days. These findings suggested that the nanoplatform exhibited minimal acute side effects and demonstrated good biocompatibility.

Conclusion

In summary, we successfully designed and synthesized the $MnO_2/Pt@BSA$ nanoplatform that exhibits excellent biocompatibility and high stability in various physiological solutions and storage conditions. To the best of our knowledge, this is the first study to use glucose and ammonia as reducing agents for potassium permanganate and platinum (IV) chloride. Through extensive research, we thoroughly explored the multifunctionality of MnO_2 and Pt in response to the tumor microenvironment and addressed the challenges of clinical radiotherapy.

In this nanoplatform system, each component had multiple functions. MnO_2 not only mediates catalytic oxygen generation but also produces Mn^{2+} as a cascade product, which enhances the Fenton-like reaction and generates additional •OH radicals, Mn^{2+} obtained from MnO_2 degradation enables MR T1-weighted imaging for enhanced cancer imaging and therapy. On the other hand, Pt not only physically enhances radiation therapy but also mediates catalytic oxygen generation. The $MnO_2/Pt@BSA$ nanoplatform demonstrated enhanced radiation therapy in U87-tumor bearing mouse model, making it a promising candidate for improving radiotherapy outcomes. However, it is important to note that this study focused solely on investigating the effects of oxygen and free radicals on tumors, and did not consider the impact of combined chemotherapy drugs, which is a limitation of our study. In future investigations, we will aim to integrate chemotherapeutic drugs into this system to achieve synergistic therapeutic effects. Additionally, recent studies have highlighted the critical role of Mn^{2+} in immunotherapy, particularly in augmenting the cGAS/STING pathway, which presents an exciting discovery for tumor therapy, particularly for glioma.[51–53] Further in-depth studies will be conducted to further investigate this observation in combination with radiotherapy.[53] In addition, we discovered that MnO_2 exhibited greater reactivity with GSH than a slightly acidic H_2O_2 microenvironment. This characteristic is highly advantageous for its application in the tumor microenvironment. Once GSH is preferentially consumed, free radicals and oxidative byproducts such as •OH radicals and oxygen are no longer depleted. Consequently, Mn^{2+} can engage in a dynamic cascade catalysis, whereas Pt simultaneously catalyzes H_2O_2. This allows for simultaneous reactions of different substrates, leading to an enhanced reaction efficiency. However, further investigations are required to fully understand the reaction kinetics involved in this process. Overall, our study contributes to the development of a highly versatile nanoplatform with great potential for improving cancer treatments. Future studies should focus on optimizing combination therapies, integrating chemotherapeutic drugs, and investigating the immunotherapeutic of this system.

Acknowledgment

Funding

Disclosure

The authors report no conflicts of interest in this work.

References

1. Gregory JV, Kadiyala P, Doherty R, et al. Systemic brain tumor delivery of synthetic protein nanoparticles for glioblastoma therapy. *Nat Commun*. 2020;11:5687. doi:10.1038/s41467-020-19225-7

2. Moliterno Günel J, Piepmeier JM, Baehring JM. *Malignant Brain Tumors: State-of-The-Art Treatment*. Berlin, Germany: Springer; 2016.

3. Lv B, Zhang H, Zheng X, et al. Structure-oriented catalytic radiosensitization for cancer radiotherapy. *Nano Today*. 2020;35:100988. doi:10.1016/j.nantod.2020.100988

4. Park JH, Lee HK. Current understanding of hypoxia in glioblastoma multiforme and its response to immunotherapy. *Cancers*. 2022;14:1176. doi:10.3390/cancers14051176

5. Liu F, Gong S, Shen M, et al. A glutathione-activatable nanoplatform for enhanced photodynamic therapy with simultaneous hypoxia relief and glutathione depletion. *Chem Eng J*. 2021;403:126305. doi:10.1016/j.cej.2020.126305

6. Li Y, Zhao P, Gong T, et al. Redox dyshomeostasis strategy for hypoxic tumor therapy based on DNAzyme-loaded electrophilic ZIFs. *Angew Chem Int Ed*. 2020;59:22537–22543. doi:10.1002/anie.202003653

7. Li R, Wang H, Liang Q, Chen L, Ren J. Radiotherapy for glioblastoma: clinical issues and nanotechnology strategies. *Biomater Sci*. 2022;10:892–908. doi:10.1039/d1bm01401c

8. Song G, Cheng L, Chao Y, Yang K, Liu Z. Emerging nanotechnology and advanced materials for cancer radiation therapy. *Adv Mater*. 2017;29:1700996. doi:10.1002/adma.201700996

9. Suh JH, Stea B, Nabid A, et al. Phase III study of efaproxiral as an adjunct to whole-brain radiation therapy for brain metastases. *J clin oncol*. 2006;24:106–114. doi:10.1200/JCO.2004.00.1768

10. Bennett MHFJSR, Milross C, Smee R, Milross C. Hyperbaric oxygenation for tumour sensitisation to radiotherapy. *Cochrane Database Syst Rev*. 2018;4:CD005007. doi:10.1002/14651858.CD005007.pub4

11. Wang H, Li J, Wang Y, et al. Nanoparticles-mediated reoxygenation strategy relieves tumor hypoxia for enhanced cancer therapy. *J Contr Rel*. 2020;319:25–45. doi:10.1016/j.jconrel.2019.12.028

12. Shen S, Chao Y, Dong Z, et al. Bottom-up preparation of uniform ultrathin rhenium disulfide nanosheets for image-guided photothermal radiotherapy. *Adv Funct Mater*. 2017;27:1700250. doi:10.1002/adfm.201700250

13. Hu Y, Zhong Z, Lu M, et al. Biomimetic O_2-carrying and highly in-situ H_2O_2 generation using Ti_3C_2 MXene/MIL-100(Fe) hybrid via Fe-Protoporphyrin bridging for photo-fenton synergistic degradation of thiacloprid. *Chem Eng J*. 2022;450:137964. doi:10.1016/j.cej.2022.137964

14. Prasad P, Gordijo CR, Abbasi AZ, et al. Multifunctional albumin–MnO_2 nanoparticles modulate solid tumor microenvironment by attenuating hypoxia, acidosis, vascular endothelial growth factor and enhance radiation response. *ACS Nano*. 2014;8:3202–3212. doi:10.1021/nn405773r

15. Li H, Cai X, Yi T, et al. Tumor microenvironment responsive Mn_3O_4 nanoplatform for in vivo real-time monitoring of drug resistance and photothermal/chemodynamic synergistic therapy of gastric cancer. *J Nanobiotech*. 2022;20:240. doi:10.1186/s12951-022-01441-6

16. Zhang R, Chen L, Liang Q, et al. Unveiling the active sites on ferrihydrite with apparent catalase-like activity for potentiating radiotherapy. *Nano Today*. 2021;41:101317. doi:10.1016/j.nantod.2021.101317

17. Nie Y, Li D, Peng Y, et al. Metal organic framework coated MnO_2 nanosheets delivering doxorubicin and self-activated DNAzyme for chemo-gene combinatorial treatment of cancer. *Int J Pharm*. 2020;585:119513. doi:10.1016/j.ijpharm.2020.119513

18. Zeng D, Wang L, Tian L, Zhao S, Zhang X, Li H. Synergistic photothermal/photodynamic suppression of prostatic carcinoma by targeted biodegradable MnO_2 nanosheets. *Drug Deliv*. 2019;26:661–672. doi:10.1080/10717544.2019.1631409

19. Liu J, Meng L, Fei Z, Dyson PJ, Zhang L. On the origin of the synergy between the Pt nanoparticles and MnO_2 nanosheets in Wonton-like 3D nanozyme oxidase mimics. *Biosens Bioelectron*. 2018;121:159–165. doi:10.1016/j.bios.2018.08.004

20. Liu J, Chen Q, Zhu W, et al. Nanoscale-coordination-polymer-shelled manganese dioxide composite nanoparticles: a multistage Redox/pH/H_2O_2-responsive cancer theranostic nanoplatform. *Adv Funct Mater*. 2017;27:1605926. doi:10.1002/adfm.201605926

21. Bi H, Dai Y, Yang P, et al. Glutathione and H_2O_2 consumption promoted photodynamic and chemotherapy based on biodegradable MnO_2–$Pt@Au_{25}$ nanosheets. *Chem Eng J*. 2019;356:543–553. doi:10.1016/j.cej.2018.09.076

22. Yi X, Chen L, Zhong X, et al. Core–shell $Au@MnO_2$ nanoparticles for enhanced radiotherapy via improving the tumor oxygenation. *Nano Res*. 2016;9:3267–3278. doi:10.1007/s12274-016-1205-8

23. Hua Y, Huang J-H, Shao Z-H, et al. Composition-dependent enzyme mimicking activity and radiosensitizing effect of bimetallic clusters to modulate tumor hypoxia for enhanced cancer therapy. *Adv Mater*. 2022;34:2203734. doi:10.1002/adma.202203734

24. Li Y, Yun K-H, Lee H, Goh S-H, Suh Y-G, Choi Y. Porous platinum nanoparticles as a high-Z and oxygen generating nanozyme for enhanced radiotherapy in vivo. *Biomaterials*. 2019;197:12–19. doi:10.1016/j.biomaterials.2019.01.004

25. Zhang F, Feng L, Jia C, et al. Mixed-valence Pt(0)/Pt^{2+} nanoassemblies as high-Z radiosensitizers and metallo-immune regulators for potent radiotherapy of breast cancer. *Nano Today*. 2023;48:101708. doi:10.1016/j.nantod.2022.101708

26. Chen M, Xie Y, Luo Q, et al. Switchable nanoparticles complexing cisplatin for circumventing glutathione depletion in breast cancer chemotherapy. *Chin Chem Lett*. 2023;34:107744. doi:10.1016/j.cclet.2022.107744

27. Fu C, Duan X, Cao M, et al. Targeted magnetic resonance imaging and modulation of hypoxia with multifunctional hyaluronic acid-MnO_2 nanoparticles in glioma. *Adv Healthc Mater*. 2019;8:1900047. doi:10.1002/adhm.201900047

28. Zheng J, Chen SH, Huang B, Zhang M, Yuan Q, Cui R. Imaging-guided precision oncotherapy mediated by nanoprobes: from seeing to curing. *Chin Chem Lett*. 2024;35(1):108460. doi:10.1016/j.cclet.2023.108460

29. Choi J, Kim G, Cho SB, Im HJ. Radiosensitizing high-Z metal nanoparticles for enhanced radiotherapy of glioblastoma multiforme. *J Nanobiotech*. 2020;18:1–23. doi:10.1186/s12951-020-00684-5

30. Xu W, Jiao L, Yan H, et al. Glucose oxidase-integrated metal-organic framework hybrids as biomimetic cascade nanozymes for ultrasensitive glucose biosensing. *ACS Appl Mater Interfaces*. 2019;11:22096–22101. doi:10.1021/acsami.9b03004

31. Lyu M, Zhu D, Kong X, et al. Glutathione-depleting nanoenzyme and glucose oxidase combination for hypoxia modulation and radiotherapy enhancement. *Adv Healthc Mater*. 2020;9:1901819. doi:10.1002/adhm.201901819

32. Chen L, Gao H, Bai Y, et al. Colorimetric biosensing of glucose in human serum based on the intrinsic oxidase activity of hollow MnO_2 nanoparticles. *New J Chem*. 2020;44:15066–15070. doi:10.1039/d0nj02387f

33. Wang D, He IW, Liu J, et al. Missing-linker-assisted artesunate delivery by metal–organic frameworks for synergistic cancer treatment. *Angewandte Chemie - Int Ed*. 2021;60:26254–26259. doi:10.1002/anie.202112128

34. Guan S, Li W, Ma J, Liu Q, Chen K, Zhang Q. Potassium-promoted three-dimensional mesoporous Pt/MnO_2 for formaldehyde elimination at zero degree. *J Chem Soc Pak*. 2020;42:188–203. doi:10.52568/000638/jcsp/42.02.2020

35. Yang X, Xiang J, Su W, et al. Modulating Pt nanozyme by using isolated cobalt atoms to enhance catalytic activity for alleviating osteoarthritis. *Nano Today*. 2023;49:101809. doi:10.1016/j.nantod.2023.101809

36. Jiang F, Yang C, Ding B, et al. Tumor microenvironment-responsive MnSiO$_3$-Pt@BSA-Ce6 nanoplatform for synergistic catalysis-enhanced sonodynamic and chemodynamic cancer therapy. *Chin Chem Lett*. 2022;33:2959–2964. doi:10.1016/j.cclet.2021.12.096

37. Xu Q, Zhang Y, Yang Z, et al. Tumor microenvironment-activated single-atom platinum nanozyme with H$_2$O$_2$ self-supplement and O$_2$-evolving for tumor-specific cascade catalysis chemodynamic and chemoradiotherapy. *Theranostics*. 2022;12:5155. doi:10.7150/thno.73039

38. Chang M, Wang M, Wang M, et al. A multifunctional cascade bioreactor based on hollow-structured Cu$_2$MoS$_4$ for synergetic cancer chemo-dynamic therapy/starvation therapy/phototherapy/immunotherapy with remarkably enhanced efficacy. *Adv Mater*. 2019;31:1905271. doi:10.1002/adma.201905271

39. Ozougwu JC. The role of reactive oxygen species and antioxidants in oxidative stress. *Int J Res Pharm Biosci*. 2016;3:1–8. doi:10.1093/braincomms/fcad356

40. Birben E, Sahiner UM, Sackesen C, Erzurum S, Kalayci O. Oxidative stress and antioxidant defense. *World Allergy Organ J*. 2012;5:9–19. doi:10.1097/WOX.0b013e3182439613

41. Xie C, Zhang T, Fu Y, Han G, Li X. CaCO$_3$-MnSiOx hybrid particles to enable CO2-mediated combinational tumor therapy. *Nano Res*. 2022;15:8281–8290. doi:10.1007/s12274-022-4471-7

42. Fu LH, Wan Y, Qi C, et al. Nanocatalytic theranostics with glutathione depletion and enhanced reactive oxygen species generation for efficient cancer therapy. *Adv Mater*. 2021;33(7):2006892. doi:10.1002/adma.202006892

43. Wu Q, Chen G, Gong K, et al. MnO$_2$-laden black phosphorus for MRI-guided synergistic PDT, PTT, and chemotherapy. *Matter*. 2019;1:496–512. doi:10.1016/j.matt.2019.03.007

44. Lai Y, Wang J, Yue N, et al. Glutathione peroxidase-like nanozymes: mechanism, classification, and bioapplication. *Biomater Sci*. 2023;11:2292–2316. doi:10.1039/d2bm01915a

45. Chen S, Yu S, Du Z, et al. Synthesis of mitochondria-anchored nitroimidazoles with a versatile NIR fluorophore for hypoxic tumor-targeting imaging and chemoradiotherapy. *J Med Chem*. 2021;64:3381–3391. doi:10.1021/acs.jmedchem.0c02250

46. Rezaee M, Sanche L, Hunting DJ. Cisplatin enhances the formation of DNA single- and double-strand breaks by hydrated electrons and hydroxyl radicals. *Radiat Res*. 2013;179:323–331. doi:10.1667/RR3185.1

47. Dong Y, Zhou L, Tian Q, Zheng Y, Sanche L. Chemoradiation cancer therapy: molecular mechanisms of cisplatin radiosensitization. *J Phys Chem C*. 2017;121:17505–17513. doi:10.1021/acs.jpcc.7b05271

48. Qi D, Xing L, Shen L, et al. A GSH-depleted platinum(IV) prodrug triggers ferroptotic cell death in breast cancer. *Chin Chem Lett*. 2022;33:4595–4599. doi:10.1016/j.cclet.2022.03.105

49. Zhang C, Qin WJ, Bai XF, Zhang XZ. Nanomaterials to relieve tumor hypoxia for enhanced photodynamic therapy. *Nano Today*. 2020;35:100960. doi:10.1016/j.nantod.2020.100960

50. Zhang Z, Wang R, Huang X, et al. Self-delivered and self-monitored chemo-photodynamic nanoparticles with light-triggered synergistic antitumor therapies by downregulation of HIF-1α and Depletion of GSH. *ACS Appl Mater Interfaces*. 2020;12:5680–5694. doi:10.1021/acsami.9b23325

51. Wang C, Xiao Y, Zhu W, et al. Photosensitizer-modified MnO$_2$ nanoparticles to enhance photodynamic treatment of abscesses and boost immune protection for treated mice. *Small*. 2020;16:2000589. doi:10.1002/smll.202000589

52. Wang C, Sun Z, Zhao C, et al. Maintaining manganese in tumor to activate cGAS-STING pathway evokes a robust abscopal anti-tumor effect. *J Control Release*. 2021;331:480–490. doi:10.1016/j.jconrel.2021.01.036

53. Yu X, Ma H, Xu G, Liu Z. Radiotherapy assisted with biomaterials to trigger antitumor immunity. *Chin Chem Lett*. 2022;33:4169–4174. doi:10.1016/j.cclet.2022.02.049